Two-Phase Displacement Interface Instability Parameterized Simulation Exploration

Wang Li[1], Yin Hang[1], Sun Tianyu[1], Li Bo[1], Sun Tiansheng[1], Shen Yanguo[2]
[1]Yingkou Institute of Technology, Yingkou, Liaoning, China
[2]Cosco shipping Crew Management (Tianjin) Co., LTD., Tianjin, China

Abstract: The application of fluid dynamics and interface phenomena in multiple industrial domains has been expanding continuously, and the demand for in-depth research has become increasingly prominent. Particularly, the fractal finger phenomenon, which is characterized by its complex multi-physical attributes, poses challenges to traditional experimental and theoretical approaches. This paper primarily proposes a finite element simulation method implemented through COMSOL Multiphysics software, with the aim of conducting a comprehensive analysis of the fractal finger phenomenon. Through the simulation, we are able to delve deeply into the underlying physical mechanisms of this phenomenon, including factors such as fluid dynamics, heat exchange, and interfacial tension. Simultaneously, the highly customizable nature of COMSOL offers us a platform for making detailed comparisons with experimental results, thereby validating the accuracy of the model. The core novelty of this paper lies in the employment of COMSOL to provide an efficient and accurate simulation strategy for the complex fractal finger phenomenon, presenting a new perspective and methodology for research in related fields.

Keywords: Fractal Finger; COMSOL Multiphysics; Finite Element Simulation; Fluid Interface Phenomenon

1. Introduction

At micro- and nanoscale levels, the study of fluid dynamics has assumed a central role in coating technology, materials science, and printed electronics. Specific fluid patterns, such as "fractal fingering" (as shown in Figure 1), offer a unique perspective for investigating these microscopic processes. The formation of such patterns is closely tied to the physical properties of the fluid, the chemical characteristics of the coating, and their interactions, with particular significance in complex multiphase flows or three-phase displacement processes. For technological applications such as high-performance coatings, superhydrophobic surfaces, and efficient optoelectronic materials, precise control of microstructures is critical. Among these, the well-known "fractal fingering" pattern, a hallmark of fractal phenomena, provides a pathway to understanding these intricate processes.

Significant research progress has been achieved in various directions concerning the displacement processes between two-phase fluids. Notably, researcher Li Yanshen, through experiments and simulations, identified the influence of gravitational effects with a stable density gradient on the fluid displacement process[1]. Huang Jianlin, Song Guangyi, and their team investigated the impact of viscosity on interfacial instability of droplets in gas-liquid two-phase systems[2]. Scholars Sun Beibei, Ye Wenhua, and others conducted numerical simulations to analyze the growth of Richtmyer-Meshkov instability at fluid interfaces[3]. Zhang Shengbo and his team employed two-dimensional unsteady Euler equations to numerically simulate the Richtmyer-Meshkov instability induced by planar shock waves interacting with interfaces of varying compositions[4]. Additionally, researcher Liu Bin utilized the Boltzmann method to study the late-stage growth of Rayleigh-Taylor instability in three-dimensional scales[5].

In the domain of numerical simulation for two-phase displacement processes, various scholars have proposed distinct research approaches and findings. Ma Cong and colleagues, focusing on coupled interfacial tension, employed the Boltzmann method to conduct simulation studies of three-dimensional fluid interfaces[6]. Guo Hailong and his team

 Copyright @ STEMM Institute Press

utilized the interface tracking method to simulate interfacial instability in immiscible fluids[7]. Yao Mengjun investigated the motion states of multiphase flows under different temperature boundary conditions through simulations[8]. Wang Xiaoying and her team explored the unique properties of liquids, analyzing interfacial instability between discrete-phase liquids (e.g., deionized water and biodiesel) and continuous-phase liquids under the influence of needle-plate electrodes[9]. Furthermore, Liu Cheng adopted an axisymmetric approach and developed a three-phase flow lattice Boltzmann model to compute interfacial stability[10].

Figure 1. Schematic Diagram of the Fingering Phenomenon Observed in Experiments

2. Mechanisms of Fractal Fingering Formation and Dynamic Model Analysis

2.1 Overview of Fractal Fingering Formation Mechanisms and Origin Analysis

In the field of fluid dynamics, the interfacial behavior of multiphase flows frequently exhibits rich and complex phenomena, with the formation of fractal fingering being a notable example. This phenomenon typically occurs during the interaction between a non-viscous fluid and a higher-viscosity fluid, driven by differences in their physical properties. When the non-viscous fluid displaces the higher-viscosity fluid, a pressure difference emerges at the interface, resulting in unstable fluid behavior. In the initial stage, the non-viscous fluid forms a protrusion resembling a droplet. However, under the influence of the pressure difference, this protrusion gradually deforms and branches (as shown in Figure 2).

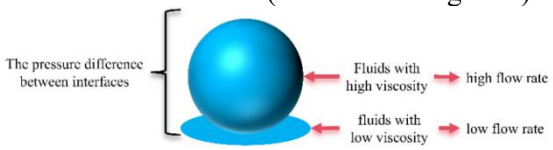

Figure 2. Schematic Diagram of the Liquid Droplet Model.

The fundamental origin of the fractal fingering phenomenon lies in fluid instability, which is primarily caused by the property differences between two fluids. This instability becomes particularly pronounced when there is a disparity between the dynamic and static pressures of the fluids.

First, fluids with different viscosities exhibit distinct flow rates. When they encounter each other in a given region, the faster-moving non-viscous fluid forms a protrusion in the contact area, attempting to bypass or penetrate the slower-moving viscous fluid (as shown in Figure 3).

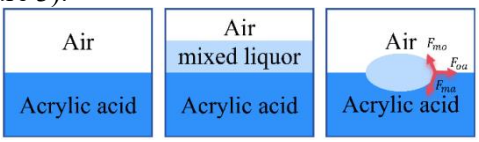

(a) Schematic Diagram of the Three-Phase Displacement Process in Droplet Dynamics

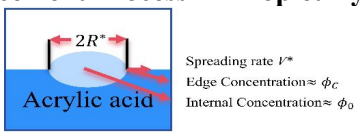

(b) Schematic Diagram of Displacement Process Parameters

Figure 3. Schematic Diagram of the Three-Phase Displacement Model

Secondly, due to friction and surface tension between the fluids, a local pressure gradient is generated, which further exacerbates the unstable behavior of the fluids. These complex interactions collectively contribute to the formation of fractal fingering, where morphological instability leads to structural branching and increased complexity.

In summary, the fractal fingering phenomenon represents a complex interfacial behavior in fluid dynamics, involving the interplay of multiple physical mechanisms, including pressure differences, dynamic and static fluid properties, friction, and surface tension.

2.2 Two-Phase Displacement Phenomenon and Mathematical Model of Its Field Environment

The basic equation of the surface tension model is given by Equation (1):

$$F_T = \gamma \cdot L \tag{1}$$

In this context, F_T denotes the surface tension force exerted on the liquid surface, (r) represents the surface tension coefficient of the liquid, and (L) indicates the line length of the liquid surface. The Navier-Stokes equations within the fluid

dynamics model govern the motion of the liquid, encompassing the mass conservation equation and the momentum conservation equation, with their specific formulations presented in Equation (2):

$$\frac{\partial \rho}{\partial t} + \nabla \cdot (\rho \boldsymbol{u}) = 0$$
$$\rho[\frac{\partial \boldsymbol{u}}{\partial t} + (\boldsymbol{u} \cdot \nabla)\boldsymbol{u}] = -\nabla p + \mu \nabla^2 \boldsymbol{u} + \boldsymbol{f} \quad (2)$$

where ρ denotes the fluid density, u the velocity field, p hydrodynamic pressure, μ dynamic viscosity, and f body forces per unit volume. Under the experimentally observed flattening of the coating surface, the morphological transition of the ink-ethanol binary system from a droplet regime to a sessile film configuration is governed by the coupled governing Equation (3):

$$\frac{\partial \alpha}{\partial t} = \frac{k_1}{S} \cdot \frac{\partial}{\partial r}(rS\frac{\partial \alpha}{\partial r}) - k_2 \alpha^2 \quad (3)$$

where α denotes the droplet number density, k_1 the pressure-driven flow coefficient, k_2 the chemical reaction rate constant, S the interfacial perimeter, and r the radial coordinate from the droplet centroid. The experimentally observed liquid vortex formation and fingering bifurcation patterns emerge fundamentally from interfacial instabilities, which are analytically described by the modified Rayleigh-Taylor instability framework as formalized in Equation (4):

$$k^2 = \frac{g\Delta\rho h}{\rho_l + \rho_h} \quad (4)$$

where k represents the dominant wavelength of interfacial instability, g the gravitational acceleration, ρ_l and ρ_h the mass densities of the lower and upper fluid layers, and h the interfacial height differential.

When ink-ethanol binary droplets impinge on a coated substrate, their capillary-driven interfacial interaction initiates a funneling flow regime governed by the following formulation. As derived from the surface tension constitutive relation (Eq. 1), the force equilibrium between capillary stresses and gravitational loading dictates droplet migration directionality. This stress balance orients the flow along the resultant surface tension vector, formally expressed as Equation (5):

$$F_T = mg \quad (5)$$

where m is the droplet mass and g gravitational acceleration. By coupling the surface tension constitutive law (Eq. 1) with the capillary-gravity stress balance (Eq. 5), the governing equation for droplet migration dynamics is derived as Equation (6):

$$\gamma \cdot L = mg \quad (6)$$

Derivation of Contact Line Length Equation (7):

$$L = \frac{mg}{\gamma} \quad (7)$$

When a droplet impacts a coated surface, the contact line length L gradually decreases due to surface tension, leading to the formation of a funnel-like structure. The morphology and scale of this funnel are governed by the surface tension coefficient (γ), droplet mass (m), and gravitational acceleration (g). Concurrently, a liquid vortex emerges during this process. By employing a three-dimensional Navier-Stokes equation in the hydrodynamic model, the governing equation for the vortex dynamics can be expressed as Equation (8):

$$\rho \cdot (\frac{\partial u}{\partial t} + u \cdot \nabla u) = -\nabla p + \mu \nabla^2 u + \rho \cdot f \quad (8)$$

where ρ, u, p, μ, and f denote fluid density, velocity field, pressure, dynamic viscosity, and external body forces, respectively. Solving these equations yields velocity and pressure fields. Interfacial instabilities arise when shear stresses act at free surfaces, generating capillary waves that amplify through mutual interactions, ultimately forming liquid vortices. These dynamics explain the capillary-driven funnel flow observed during ink-alcohol droplet deposition on coated substrates.

Fractal fingering patterns, however, deviate fundamentally from conventional three-phase immiscible displacement models. The omission of viscous coupling between phases in such models necessitates a viscoelastic constitutive framework. Viscoelastic fluids exhibit stress-dependent rheological responses unaccounted for in Newtonian approximations. Their effective viscosity (η) depends on both instantaneous strain rates (γ) and stress relaxation history. The viscoelastic behavior is modeled as Equation (9):

$$\sigma_{ij} = -p\delta_{ij} + \lambda \epsilon_{kk} \delta_{ij} + 2\mu \epsilon_{ij} \quad (9)$$

where p denotes pressure, δ_{ij} is the *Kronecker Delta* (1 if $i=j$, 0 otherwise), and λ, μ represent the Lamé coefficient and dynamic viscosity, respectively. For viscoelastic fluids, the Navier-Stokes equations can be modified as Equation (10):

$$\rho \cdot (\frac{\partial u}{\partial t} + u \cdot \nabla u) = -\nabla p + \nabla \cdot \sigma + \rho \cdot f \quad (10)$$

The viscous stress tensor σ is given by Equation (11):

$$\sigma = \mu(\nabla u + (\nabla u)^{\mathrm{T}}) + \lambda \cdot (\nabla \cdot u) \cdot I \quad (11)$$

 Copyright @ STEMM Institute Press

where I is the identity matrix, ∇ is the gradient operator, and $(\nabla u)^{\mathrm{T}}$ represents the transpose of ∇u. Therefore, the complete derivation of Model 1 incorporating the viscoelastic fluid model can be expressed as Model 2. Model 2 couples the surface tension model, hydrodynamic model and viscoelastic flow model together for more in-depth study of complex fluid flow behaviors and properties.

Considering that in the liquid droplet model, the fluid motion of internal airflow at the contact interface will affect the three-phase displacement motion, we also need to adjust parameters for geometric shape and dynamic influences. Assuming the droplet forms an annular liquid film on the plane with width $2a$, height h, film thickness d, areal density ρ, surface saturation vapor pressure P_S, gravitational acceleration g, surface tension λ, liquid viscosity coefficient μ, liquid density ρ_{liq}, and medium density beneath the annular film ρ_{gas}.

First, we assume the airflow velocity V within the annular film is sufficiently small to be negligible. The flow in the annular film can then be described using the *Navier-Stokes* equations, as shown in Equation (12):

$$\rho_{liq}(\frac{\partial u}{\partial t} + u \cdot \nabla u) = -\nabla p + \nabla \cdot \sigma + \rho_{liq} \cdot g \quad (12)$$

where u is the fluid velocity vector and g represents the gravitational acceleration vector. Assuming the liquid is a Newtonian fluid, the viscous stress tensor can be expressed by Equation (13):

$$\sigma = -p \cdot I + 2\mu \cdot \epsilon \quad (13)$$

where ϵ denotes the strain rate tensor. For liquid flow in the annular film, the non-zero components of this tensor are given by Equation (14):

$$\epsilon_{rr} = \frac{\partial u}{\partial r} \epsilon_{\theta\theta} = -\frac{u}{r} \quad (14)$$

$$\epsilon_{r\theta} = \frac{1}{2}(\frac{\partial u}{\partial \theta} + \frac{1}{r}\frac{\partial v}{\partial r}) \quad (15)$$

Therefore, the radial and angular components of the *Navier-Stokes* equations can be expressed by Equation (16):

$$\begin{aligned} \frac{\partial^2 u}{\partial r^2} + \frac{1}{r}\frac{\partial u}{\partial r} - \frac{u}{r^2} &= \frac{1}{\rho_{liq}}\frac{\partial p}{\partial r} + \frac{2}{\rho_{liq}}\frac{\partial}{\partial r}[\mu(\frac{\partial u}{\partial r} + \frac{1}{r}\frac{\partial u}{\partial \theta})] \\ \frac{1}{r^2}\frac{\partial}{\partial \theta}(r^2\frac{\partial u}{\partial \theta}) &= \frac{1}{\rho_{liq}}\frac{1}{r}\frac{\partial p}{\partial \theta} + \frac{2}{\rho_{liq}r}\frac{\partial}{\partial \theta}[\mu(\frac{\partial u}{\partial r} + \frac{1}{r}\frac{\partial u}{\partial \theta})] \end{aligned} \quad (16)$$

Assuming the fluid in the annular film is stationary (i.e., zero velocity), the coupled solution of the above two equations is given by Equation (17):

$$u(r,\theta) = -\frac{\Delta p}{4\mu}r^2(1 - \frac{a^2}{r^2}) + Vr\sin\theta \quad (17)$$

where Δp represents the pressure difference between the upper and lower surfaces of the annular film, and V denotes the airflow velocity outside the film. The liquid surface profile and droplet morphology can then be determined. The liquid surface shape is derived from a modified *Young-Laplace* formulation, accounting for internal pressure effects on surface morphology. Experimentally, the liquid film is characterized as annular. Consequently, the pressure at any point on the annular film is given by Equation (18):

$$p = p_s + \frac{\Delta p}{2} - \rho g h + \gamma(\frac{1}{r}\frac{\partial h}{\partial \theta})^2 \quad (18)$$

where p_s is the liquid's saturated vapor pressure, Δp the pressure difference across the liquid film, and h the annular film height. Using the *Young-Laplace* equation, we obtain the film's morphological equation as Equation (19):

$$\frac{1}{r}\frac{\partial}{\partial r}(r\frac{\partial h}{\partial r}) + \frac{1}{r^2}\frac{\partial^2 h}{\partial \theta^2} = \frac{1}{\gamma}[\frac{\Delta p}{2} - p_s + \rho g h - \frac{\gamma}{r}\cdot\frac{\partial^2 h}{\partial \theta^2}] \quad (19)$$

The solution of the *Young-Laplace* equation yields the film height function $h(r,0)$, which typically requires numerical methods (finite element or finite difference) or perturbation techniques due to the absence of analytical solutions. The finite element method discretizes the rigid surface into elements to solve fundamental equations locally for global solutions, while the finite difference method replaces partial derivatives with nodal differences along grids to solve discretized equations. The perturbation method obtains approximate solutions through series expansion and iterative refinement of terms at different orders.

For the perturbation approach, we solve the problem by expanding both the height function h and the corresponding pressure equations as power series. The constraint conditions for this process are specified in Equation (20):

$$h(r,\theta) = h_0(r) + \epsilon h_1(r,\theta) + \epsilon^2 h_2(r,\theta) + \ldots \quad (20)$$

where, e denotes a small parameter that is substituted into the *Young-Laplace* equation. The solution procedure involves applying boundary conditions, linearizing the governing equations, and solving the resulting ordinary differential equations to obtain hierarchical approximations of h at different perturbation orders.

3. Numerical Simulation of Two-Phase Displacement

The formation and evolution of fractal fingering

patterns represent a multiscale, multiphysics challenge in interfacial hydrodynamics. While experimental and theoretical studies have advanced significantly, accurate numerical modeling of these nonlinear phenomena remains critical. COMSOL Multiphysics provides an effective finite-element framework for such simulations, combining computational precision with robust multiphysics coupling capabilities. Our simulations reveal the underlying mechanisms governing fingering dynamics, spanning fluid flow, heat transfer, and interfacial tension effects.

COMSOL's visualization and customization capabilities enable tailored model development for direct experimental validation. Compared to conventional approaches, this numerical framework offers both deeper physical insight and computational efficiency. For the current study, we coupled the Laminar Flow and Ternary Phase Field modules, with the model geometry illustrated in Figure 4.

The simulation results are shown in Figure 5, including: (a) velocity contours of the two-phase displacement, (b) pressure variation diagram, and (c) fluid volume fraction diagram. Analysis of these figures reveals that during the displacement process, the velocity contours show the air phase velocity increases as displacement progresses, though this acceleration does not affect the pressure variation between liquids. The main driving force remains the interfacial pressure difference, which gradually decreases with time-step convergence and eventually reduces to zero when displacement is completed.

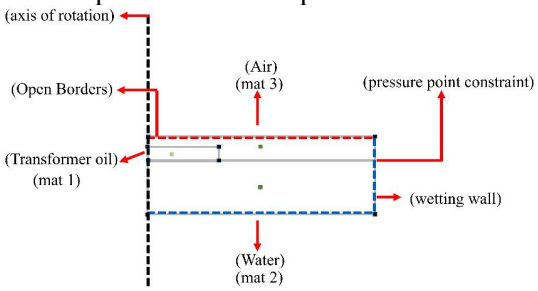

Figure 4. Schematic Diagram of the Simulation Model Geometry Setup

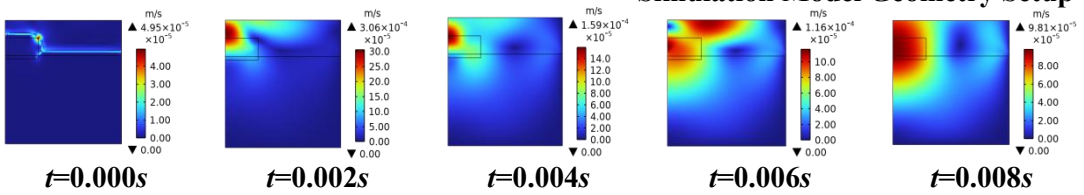

(a) Schematic Diagram of Velocity Contour Evolution

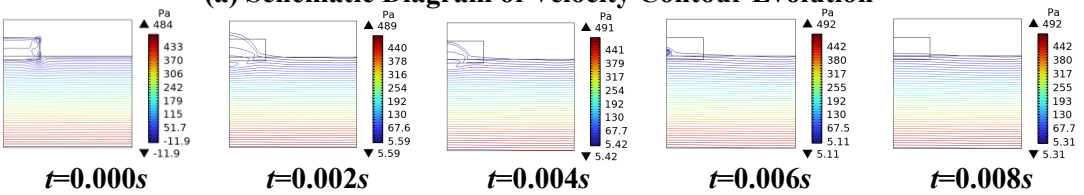

(b) Schematic Diagram of Pressure Variation

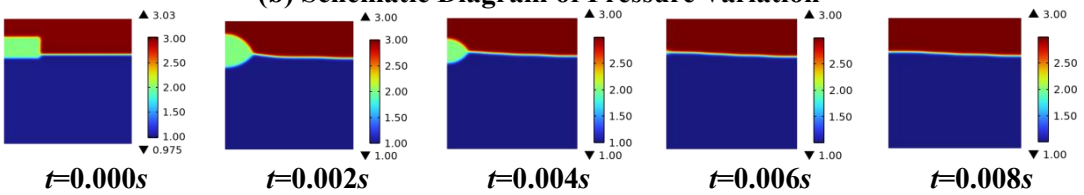

(c) Schematic Diagram of Fluid Volume Variation

Figure 5. Schematic Diagram of Simulation Results

The observation of velocity contours, pressure diagrams, and fluid motion diagrams reveals that the displacement of pressure points aligns with the aforementioned theoretical predictions, thus confirming that the main driving forces are surface tension and viscous forces.

From the top-view observation of the petri dish, the simulation results are shown in Figure 6. Analysis of the top view indicates that after the completion of the cross-sectional displacement process, the stratification process continues. Since the model was constructed by simulating the cross-section and then extending it through rotational simulation, the in-plane stratification phenomenon is not directly visible in the model. However, the annular pressure difference in the plane can be used to infer the fractal process.

 Copyright @ STEMM Institute Press

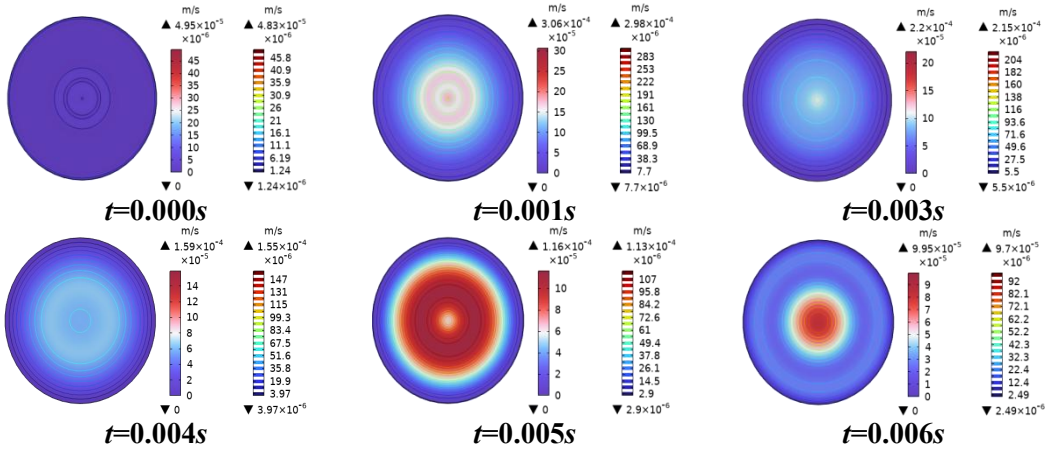

Figure 6. Schematic Diagram of 3D Perspective Simulation Results

Observation of the three-dimensional velocity contour clearly reveals distinct stratification phenomena, confirming the validity of the simulation model construction.

4. Conclusions

Based on theoretical analysis and simulation results:

Gas velocity exceeds liquid velocity during two-phase displacement, but its increase does not affect displacement efficiency.

The primary driving force originates from the interphase pressure difference, which gradually decreases until vanishing at displacement completion.

Increasing temperature accelerates fingering instability development.

Acknowledgments

2024 College Student Innovation and Entrepreneurship Training Program (National Level): Simulation and Performance Optimization of High-Voltage Switchgear Based on Digital Twin Technology (No. 202414435011).

2024 College Student Innovation and Entrepreneurship Training Program (University Level): Effect of Bubble Impurities on Partial Discharge Characteristics of Transformer Oil Engineering Liquid Dielectrics (No. X202414435027).

2024 Yingkou Institute of Technology Education and Teaching Reform Research Project (No. JG202402): Ideological and Political Teaching Design and Practice of 'College Physics' Course under Online-Offline Hybrid Teaching Mode.

References

[1] Li Yanshen. Research progress on flow instability of spherical interfaces in stable density gradients[J]. Chinese Journal of Theoretical and Applied Mechanics, 2024, 56(06): 1540-1551.

[2] Huang Jianlin, Song Guangyi, Wang Jingzhu, et al. Effect of viscosity on interface instability of cylindrical droplets induced by internal cavitation[J]. Chinese Journal of Theoretical and Applied Mechanics, 2024, 56(02): 377-386.

[3] Sun Beibei, Ye Wenhua, Zhang Weiyan. Numerical simulation of density-perturbed Richtmyer-Meshkov-like instability growth and its coupling with unperturbed interfaces[J]. Acta Physica Sinica, 2023, 72(19): 123-130.

[4] Zhang Shengbo, Zhang Huanhao, Chen Zhihua, et al. Influence of different interface component distributions on Richtmyer-Meshkov instability[J]. Acta Physica Sinica, 2023, 72(10): 248-261.

[5] Liu Bin. Late-stage growth study of three-dimensional Rayleigh-Taylor instability using lattice Boltzmann method[D]. Hangzhou Dianzi University, 2022.

[6] Ma Cong, Liu Bin, Liang Hong. Lattice Boltzmann simulation of three-dimensional fluid interface instability coupled with interfacial tension[J]. Acta Physica Sinica, 2022, 71(04): 153-163.

[7] Guo Hailong, Zhang Ying, Li Wenbin, et al. Direct numerical simulation of Kelvin-Helmholtz instability using interface tracking method[J]. Chinese Internal Combustion Engine Engineering, 2021, 42(03): 16-25. [8] Yao Mengjun. Numerical simulation of multiphase flow instability in heat collection tubes under different temperature boundary conditions[D]. Nanchang University, 2021.

Copyright @ STEMM Institute Press

[9] Wang Xiaoying, Wu Shibo, Wang Dongbao, et al. Analysis of liquid interface instability under needle-plate electrode action[J]. Journal of Jiangsu University (Natural Science Edition), 2020, 41(05): 523-529.

[10] Liu Cheng. Axisymmetric three-phase flow lattice Boltzmann model and its application in Rayleigh-Plateau instability[D]. Hangzhou Dianzi University, 2023.

 Copyright @ STEMM Institute Press